RAPINN: A novel Residual guided self-Adaptive loss balanced Physics-Informed Neural Network for robust early cancer detection

Somnath Das **Scindhiya Laxmi** *

Department of Mathematics and Computing
Indian Institute of Technology (Indian School of Mines)
Dhanbad, Jharkhand, India, 826004

Abstract

Physics-Informed Neural Networks (PINNs) have emerged as an efficient scientific deep learning framework that integrates the governing physical laws directly into the neural network training process. This is accomplished by embedding the residuals of the underlying physical equations into the loss function, evaluated at collocation points distributed across the spatio-temporal domain. Focusing on the breast tumor detection, the spatial distribution of these collocation points within the breast tissues plays a crucial role in determining the model's ability to accurately identify tumor regions. The loss function of PINNs comprises multiple components, including the residual loss corresponding to the governing equations, boundary conditions loss, and the data mismatch loss derived from the observed measurements. While optimizing the model parameters and minimizing the loss function, PINNs inherently focus more on the loss components that contribute to high values. In this work, the self-adaptive loss approach is based on parameterized weighting coefficients assigned to each loss term. We apply this adaptive weighting and adaptive domain refinement emphasizing to regions with high residuals, enabling the precise capture of steep gradient variations in critical areas. Data-driven modeling of bio-heat transfer equations has also been done using the proposed methodology. Computational simulations demonstrate that both tumor localization and shape estimation are achieved with high accuracy.

1 Introduction

Breast cancer remains a leading cause of mortality among women, though screening tests e.g., mammography, and MRI have significantly reduced death rates [Ganesan et al., 2012]. However, their limitations, such as patient discomfort, radiation exposure, limited accuracy in dense tissues, and high false positive rates[Gutierrez et al., 2024] often lead to unnecessary biopsies[Siravegna et al., 2017]. To overcome these challenges, advanced computational tools are needed for precise and non-invasive cancer detection and diagnosis. The pursuit of safe, non-invasive adjunctive methods for breast cancer detection with high precision continues to be a major research objective [Harada-Shoji et al., 2021, c. Gutierrez and Kandlikar, 2024, Mukhmetov et al., 2023].

In biomedical science engineering, Physics Informed Neural Networks (PINNs) Raissi et al. [2019] has been applied from biomechanics to medical imaging. In PINNs, the integration of the physical laws into the loss function reduce the expensive data assimilation requirement and ensure the physical relevance. However, PINNs frameworks continue to face challenges in convergence, stability, and

*Corresponding author: scindhiya@iitism.ac.in

2nd Conference on Applied AI and Scientific Machine Learning (CASML 2025).

generalization, particularly when dealing with complex and nonlinear partial differential equations (PDEs). To address these issues, numerous extensions to the baseline PINN have been proposed. For instance, meta-learning has been used to design improved loss functions [Psaros et al., 2022], and gradient-enhanced PINNs incorporate PDE-residual gradients to reduce residual loss [Yu et al., 2022].

Since in PINNs structure, the total loss is a weighted combination of PDE, initial and boundary conditions losses, several approaches have been developed to automatically tune these weights and maintain balance during training [Xiang et al., 2022], including the use of point-wise adaptive weights. For large domains, spatio-temporal decomposition has been shown to accelerate training and improve accuracy [Jagtap and Karniadakis, 2020]. In time-dependent problems, progressive training starting with a short time window and gradually expanding it often enhances learning stability [Mattey and Ghosh, 2022]. Additional problem-specific strategies, such as architectures that satisfy Dirichlet or periodic boundary conditions exactly, have also been introduced[Dong and Ni, 2021]. However, inverse modeling remains difficult: data-mismatch losses frequently fail to dominate other gradients, causing PINNs to perform poorly in inverse modeling [Zhou and Xu, 2024]. These gaps in the existing literature motivated us to advance the algorithmic foundations of PINNs and to apply the resulting robust, enhanced framework to biomedical applications, particularly breast cancer detection involving PDE-based temperature modeling, tumor growth dynamics, and bio-imaging processes.

This work aims to enhance the convergence speed and stability of bio-heat transfer model solutions by introducing a novel framework called **R**esidual guided self-**A**daptive loss balanced **P**hysics-**I**nformed **N**eural **N**etworks (RAPINN). The proposed RAPINN method is designed for robust early cancer detection and for estimating tumor location and size. The framework builds on high-residual points during training to improve learning efficiency and accuracy, while simultaneously maintaining an adaptive balance among the different loss components through a self-adjusting loss-balancing coefficient. This mechanism makes the data-driven solution, i.e., the temperature distribution in the target region accurately. Moreover, in inverse modeling, RAPINN strategically starts to pay more attention towards the data-mismatch loss term near to convergence of the reliable tuning of the unknown tumor-related parameters. This adaptive behavior makes the proposed framework an effective tool for both forward and inverse modeling in biomedical applications.

2 Methodology

In conventional loss-balanced PINNs, the residual loss weight often converges toward zero during early training, impeding model convergence. To address this challenge, the proposed methodology, RAPINN, integrates the principles of self-adaptive loss-balanced PINN [Xiang et al., 2022] with residual-based adaptive refinement with distribution PINN [Wu et al., 2023]. In this work, to prevent the convergence towards zero of the residual loss coefficient, we have initiated the adaptive loss weights after a predefined threshold. Additionally, the inverse modeling task involves estimating tumor location and diameter with high accuracy using limited surface temperature data. Comparative analysis is carried out against baseline PINN [Raissi et al., 2019], and finite difference method [Ozisik et al., 2017] to assess performance, accuracy, and robustness of the proposed framework.

We propose a unified framework termed **R**esidual-guided self-**A**daptive loss-balanced **P**hysics-**I**nformed **N**eural **N**etwork (**RA-PINN**), which combines dynamic loss-balancing with residual-driven collocation refinement to achieve efficient and stable convergence. Let the governing physical model be expressed in the general form of a partial differential equation (PDE):

$$u_t + \mathcal{N}[u](\mathbf{x}, t) = 0, \qquad \mathbf{x} \in \Omega,\ t \in [0, T], \tag{1}$$

subject to initial and boundary constraints:

$$\mathcal{I}[u](\mathbf{x}, 0) = u_0(\mathbf{x}), \qquad \mathcal{B}[u](\mathbf{x}, t) = u_b(\mathbf{x}, t),\ \ \mathbf{x} \in \partial\Omega,\ t \in [0, T]. \tag{2}$$

A fully connected neural network $\hat{u}_\theta(\mathbf{x}, t)$ parameterized by $\theta = \{W, b\}$, constructing solution field for the model. The forward propagation through l hidden layers is given by

$$\begin{aligned} h^{(0)} &= \mathbf{x}, \\ h^{(p)} &= \phi_h\left(W^{(p)} h^{(p-1)} + b^{(p)}\right), \qquad p = 1, \ldots, l, \\ \hat{u}_\theta &= \phi_o\left(W^{(l+1)} h^{(l)} + b^{(l+1)}\right), \end{aligned}$$

where ϕ_h and ϕ_o denote the activation functions of the hidden and output layers, respectively. The predicted field $\hat{u}_\theta$ is used to compute the loss components corresponding to the governing equation, constraints, and available measurement data:

$$\mathcal{L} = \mathcal{L}_{PDE} + \mathcal{L}_{IC} + \mathcal{L}_{BC} + \mathcal{L}_{data}. \tag{3}$$

To enhance sampling efficiency, RA-PINN incorporates a residual-guided distribution strategy wherein new collocation points are drawn according to the normalized PDE residual field. For the residual $\varepsilon(\mathbf{x})$ evaluated at the current iteration, the sampling density is defined as

$$p(\mathbf{x}) \propto \frac{\varepsilon^k(\mathbf{x})}{\mathbb{E}[\varepsilon^k(\mathbf{x})]} + c, \tag{4}$$

where k and c are non-negative hyper-parameters. This mechanism results in a progressively refined distribution of collocation points concentrated in regions having larger residuals.

To achieve stable training in the presence of multiple competing loss terms, RA-PINN employs a self-adaptive probabilistic formulation that treats every component of the loss as arising from an independent Gaussian likelihood. Let the model outputs corresponding to data, initial, boundary, and PDE residual constraints be represented by the four vectors u, u_0, u_b, and f, respectively. Under Gaussian assumptions with variances $\epsilon = \{\epsilon_d, \epsilon_i, \epsilon_b, \epsilon_f\}$, the joint likelihood is expressed as

$$\begin{aligned} p(u, u_0, u_b, f|\hat{u}(\mathbf{x}, t; \theta)) = N(\mathcal{F}[\hat{u}(\mathbf{x}, t; \theta)], \epsilon_f^2) \cdot N(\hat{u}(\mathbf{x}, t; \theta), \epsilon_b^2) \\ \cdot N(\hat{u}(\mathbf{x}, t; \theta), \epsilon_i^2) \cdot N(\hat{u}(\mathbf{x}, t; \theta), \epsilon_d^2) \end{aligned} \tag{5}$$

where $\mathcal{F}[\hat{u}_\theta]$ denotes the PDE residual operator. Minimizing the negative log-likelihood leads to the multi-objective loss:

$$\begin{aligned} -\log p(u, u_0, u_b, f \mid \hat{u}_\theta) = \frac{1}{2\epsilon_f^2}\mathcal{L}_{PDE} + \frac{1}{2\epsilon_b^2}\mathcal{L}_{BC} + \frac{1}{2\epsilon_i^2}\mathcal{L}_{IC} \\ + \frac{1}{2\epsilon_d^2}\mathcal{L}_{data} + \log(\epsilon_d\epsilon_i\epsilon_b\epsilon_f). \end{aligned} \tag{6}$$

Introducing logarithmic variances $s = \log \epsilon^2$ with $s = \{s_d, s_i, s_b, s_f\}$, the adaptive loss for RA-PINN becomes

$$\begin{aligned} \mathcal{L}(s; \theta) = \frac{1}{2}e^{-s_f}\mathcal{L}_{PDE} + \frac{1}{2}e^{-s_b}\mathcal{L}_{BC} + \frac{1}{2}e^{-s_i}\mathcal{L}_{IC} \\ + \frac{1}{2}e^{-s_d}\mathcal{L}_{data} + \frac{1}{2}(s_f + s_b + s_i + s_d). \end{aligned} \tag{7}$$

To prevent premature vanishing of the residual-weight coefficient, RA-PINN activates the adaptive parameters only after a predefined training threshold. Before this threshold, all loss components are maintained with fixed weights, ensuring the network adequately learns the global structure of the solution before adaptive balancing begins.

Figure 2 illustrates the RA-PINN workflow, wherein residual-guided sampling and adaptive loss-weight updates operate jointly with neural network training to obtain a stable and accurate solution for the underlying physical system.

$$\begin{aligned} \mathcal{L}(s; \theta; N) = \frac{1}{2}e^{-s_f}\,\mathcal{L}_{PDE}(\theta; N_f) + \frac{1}{2}e^{-s_b}\,\mathcal{L}_{BC}(\theta; N_b) + \frac{1}{2}e^{-s_i}\,\mathcal{L}_{IC}(\theta; N_i) \\ + \frac{1}{2}e^{-s_d}\,\mathcal{L}_{data}(\theta; N_{data}) + \frac{s_f}{2} + \frac{s_b}{2} + \frac{s_i}{2} + \frac{s_d}{2} \end{aligned}$$

In self adaptive loss-balanced PINN, the residual loss weight often converges toward zero during early training, impeding model convergence. Hence, the proposed methodology prevents the convergence towards zero of the residual loss coefficient. Here, we have initiated the adaptive loss weights after a predefined threshold.
Here in Figure2, a diagram of RA-PINN for predicting the temperature distribution of the breast cancer model is attached:

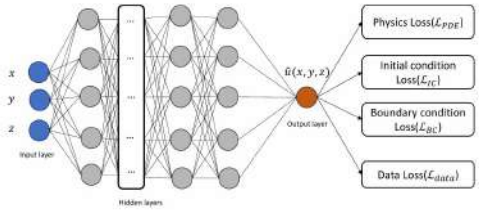

Figure 1: Physics-Informed Neural Network Architecture

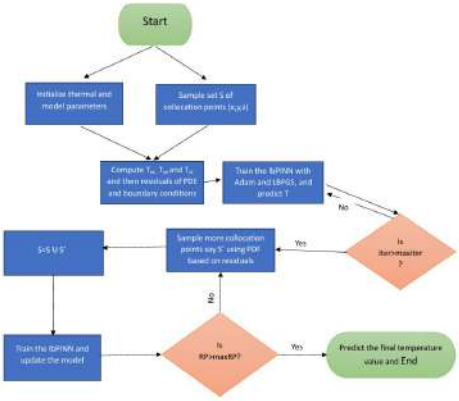

Figure 2: Flowchart of the RA-PINN Algorithm

3 RA-PINN for forward thermal modeling of breast tumors

To evaluate the performance of the proposed method for early cancer detection, the framework is validated across several scenarios. In the forward problem setting, the RA-PINN framework is employed to model breast thermal dynamics based on Penne's bioheat transfer equation [Gonzalez-Hernandez et al., 2020], with the clinical goal of improving early-stage breast cancer detection. Within this framework, tumors are represented as metabolically active and highly perfused heat sources embedded within the breast tissue.

The thermal response of the tissue domain is governed by the following equation:

$$\frac{\partial T}{\partial t} = k\left(\frac{\partial^2 T}{\partial x^2} + \frac{\partial^2 T}{\partial y^2} + \frac{\partial^2 T}{\partial z^2}\right) + \rho_b c_b \omega_b (T_a - T) + Q, \tag{8}$$

with boundary conditions:

$$T_A = T_{body} \tag{9}$$

$$-k\frac{\partial T}{\partial n}\bigg|_B = h(T - T_\infty) \tag{10}$$

where n is the unit normal vector, h is the heat transfer coefficient, T_{body} is the core body temperature, and T_∞ is the ambient body temperature.

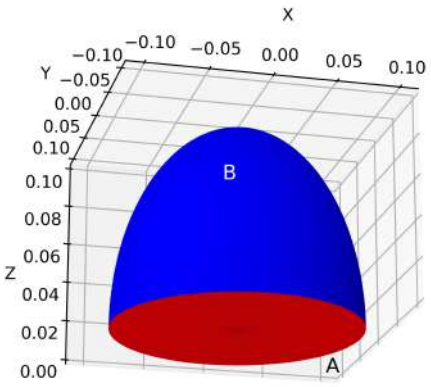

Figure 3: Synthetic 3D geometry

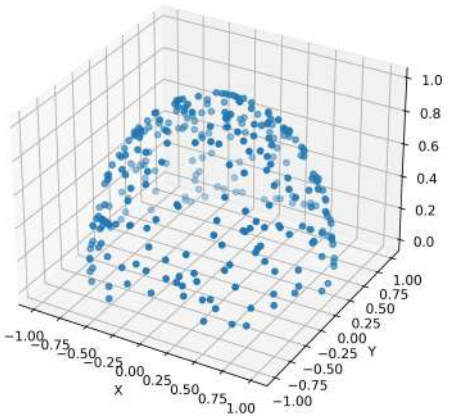

Figure 4: Surface boundary points on the defined geometry

Values of the thermal PDE parameters in equations 8,-10 are discussed in Table 1. For the detailed discussion, readers are referred to the work of González-Hernández et al. [Gutierrez and Kandlikar, 2025].

Table 1: Thermal parameters used in thermal simulations for breast cancer.

Notation	Definition	Value (SI units)
k	Thermal conductivity	$0.42\ \mathrm{W\,m^{-1}\,K^{-1}}$
w_h	Perfusion rate of healthy tissue	$1.8 \times 10^{-4}\ \mathrm{s^{-1}}$
w_t	Perfusion rate of tumor	$9 \times 10^{-3}\ \mathrm{s^{-1}}$
Q_h	Metabolic heat of healthy tissue	$450\ \mathrm{W\,m^{-3}}$
Q_t	Metabolic heat of tumor	$8.7 \times 10^{3} - 6.54 \times 10^{4}\ \mathrm{W\,m^{-3}}$
c_b	Specific heat of blood	$3840\ \mathrm{J\,kg^{-1}\,K^{-1}}$
ρ_b	Density of blood	$1060\ \mathrm{kg\,m^{-3}}$
T_a	Arterial temperature	310 K
T_∞	Ambient temperature	298 K

The values of Q and ω are specified as follows:

$$Q = \begin{cases} \dfrac{3.27 \times 10^{6}}{468.5 \times \ln(100 d_{\text{tumor}}) + 50}, & \text{if } (x, y, z) \in \text{tumor region} \\ 450, & \text{if } (x, y, z) \notin \text{tumor region} \end{cases} \tag{11}$$

and

$$\omega = \begin{cases} 9 \times 10^{-3}, & \text{if } (x, y, z) \in \text{tumor region} \\ 1.8 \times 10^{-4}, & \text{if } (x, y, z) \notin \text{tumor region} \end{cases} \tag{12}$$

4 Experimental setup and simulation

We employ the prpposed RA-PINN to solve the $3D$ Penne's bioheat equation [Gonzalez-Hernandez et al., 2020] on a hemispherical domain with radius 0.1m, tumors of different diameters (say d) are present at three distinct locations (say loc). The network is initially trained using the L-BFGS optimizer [Le et al., 2011] for a small number of epochs to achieve rapid loss reduction, then followed by Adam [Kingma and Ba, 2014] optimizer, and again L-BFGS has been applied to avoid loss oscillations.

4.1 Set up for forward simulation

These equations and conditions are incorporated directly into the loss function of the proposed model, which is defined as follows:

$$\mathcal{L}_{PDE}(\hat{T}, \theta) = \frac{1}{N_f} \sum_{i=1}^{N_f} \left|\left| k\left(\frac{\partial^2 \hat{T}_i}{\partial x^2} + \frac{\partial^2 \hat{T}_i}{\partial y^2} + \frac{\partial^2 \hat{T}_i}{\partial z^2} \right) + \rho_b c_b w_b (T_a - \hat{T}_i) + Q \right|\right|_2^2, \text{ and}$$

$$\mathcal{L}_{BC}(\hat{T}, \theta) = \frac{1}{N_A} \sum_{j=1}^{N_A} ||\hat{T}_j - T_a||_2^2 + \frac{1}{N_B} \sum_{j=1}^{N_B} \left|\left| k \frac{\partial \hat{T}_j}{\partial n} - h(\hat{T}_j - T_\infty) \right|\right|_2^2$$

where $\hat{T}$ is the output from the network, N_f is the number of collocation points inside the domain, and N_A and, N_B are the number of data points corresponding to boundary sides A and B, respectively. The total loss of the model is given as:

$$\mathcal{L}(s; \theta) = \frac{1}{2} \exp(-s_f) \mathcal{L}_{PDE}(\hat{T}, \theta) + \frac{1}{2} \exp(-s_b) \mathcal{L}_{BC}(\hat{T}, \theta) + \frac{s_f}{2} + \frac{s_b}{2}$$

The loss function then utilizes the optimizers to obtain the final model parameters that will yield a final predicted temperature distribution. In the forward simulation, tumors were placed at three defined locations: L1 (0, 0, 0.07), L2 (0, 0, 0.04), and L3 (0, 0.025, 0.07). Two tumor sizes were tested, S1 (10 mm) and S2 (20 mm), alongside a non-tumor case with standard tissue metabolic and blood perfusion rates, yielding a total of seven cases.

4.2 Set up for inverse simulation

The inverse simulation aimed to estimate the tumor's location and diameter based on the surface temperature of the hemisphere, which was derived from the forward RA-PINN solutions for seven cases.

The total loss of the inverse simulation is given as:

$$\begin{aligned}\mathcal{L}(s;\theta) = &\frac{1}{2}e^{-s_f}\,\mathcal{L}_{PDE}(\hat{T},\theta) + \frac{1}{2}e^{-s_b}\,\mathcal{L}_{BC}(\hat{T},\theta) + \frac{1}{2}e^{-s_d}\,\mathcal{L}_{data}(\hat{T},\theta)\\ &+ \frac{s_f}{2} + \frac{s_b}{2} + \frac{s_d}{2}\end{aligned} \tag{13}$$

In the inverse modeling process, the findings of Gautherie [Gautherie, 1980] were used to set physiological constraints. From Equation 11, the minimum detectable tumor diameter was determined to be 0.01 m (10 mm). Therefore, a lower bound of 0.01 m was imposed on the tumor diameter. Similarly, the maximum diameter was limited to 0.05 m (50 mm), considering the model size and the spatial extent of the breast. Additionally, the tumor center was constrained to remain within the breast region. To enforce these conditions, a penalty function was introduced for the tumor center coordinates (x, y, z).

$$\text{penalty} = \text{sphere violation}(x, y, z) + \text{diameter violation}(x, y, z)$$

Where

$$\text{sphere violation} = Max(0, x^2 + y^2 + z^2 - 0.1^2)$$

and

$$\text{diameter violation}(x, y, z) = Max(0, 0.01 - \text{tumor diameter}) + Max(0, \text{tumor diameter} - 0.05)$$

The total loss of the inverse simulation is given as:

$$\begin{aligned}\mathcal{L}(s;\theta) = &\frac{1}{2}e^{-s_f}\,\mathcal{L}_{PDE}(\hat{T},\theta) + \frac{1}{2}e^{-s_b}\,\mathcal{L}_{BC}(\hat{T},\theta) + \frac{1}{2}e^{-s_d}\,\mathcal{L}_{data}(\hat{T},\theta)\\ &+ \frac{s_f}{2} + \frac{s_b}{2} + \frac{s_d}{2} + \lambda \cdot penalty\end{aligned} \tag{14}$$

In Equation 14, λ denotes the penalty coefficient in the loss function. Figure 5 and 6 shows two diagrams demonstrating the convergence of the predicted tumor diameter and center to the true values.

5 Results and discussions

The proposed RA-PINN was applied to the three-dimensional Pennes bioheat equation [Gonzalez-Hernandez et al., 2020] on a hemispherical domain (radius $R = 1$). We considered tumors of varying diameters positioned at three candidate locations; the training protocol combined a short L-BFGS warm-start [Le et al., 2011] for rapid initial descent, a longer Adam stage [Kingma and Ba, 2014] for robust optimization, and a final L-BFGS refinement to reduce oscillations and polish the solution.

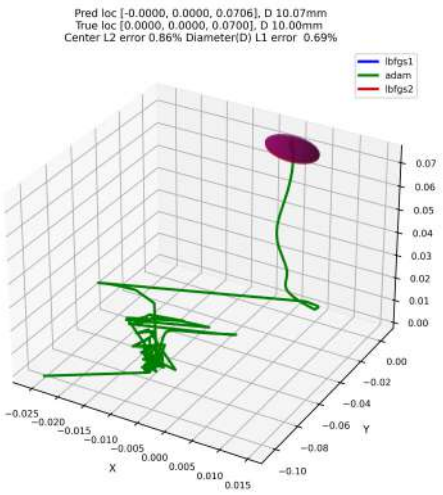

Figure 5: Tumor center simulation for the case L1S1

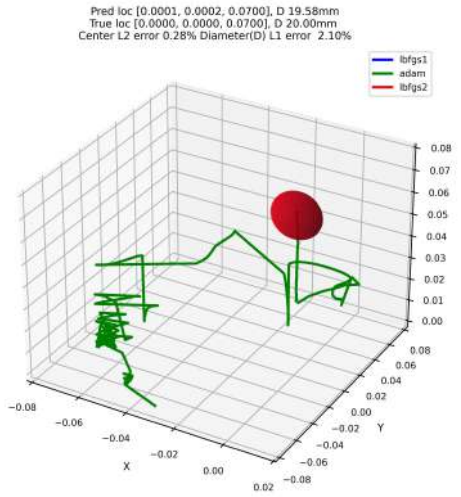

Figure 6: Tumor center simulation for the case L1S2

5.1 Forward modeling

Table 2 summarizes the seven forward test cases (six tumor cases plus a healthy reference) together with representative RAPINN boundary and residual losses. The forward PINN enforces the bioheat PDE and boundary conditions through the adaptive loss in Eq. (13), while residual-guided sampling concentrates collocation points in regions of high model error to improve local accuracy.

Figure 7 shows the total loss and the evolution of adaptive loss-weights for case L1S1, demonstrating the stabilizing effect of the staged optimization schedule. Surface temperature predictions for the L1, L2 and L3 configurations are presented in Figures 8–13; these panels illustrate the temperature signatures produced by tumor size and depth variations and highlight where residual-driven refinement had the largest impact.

Table 2: Actual tumor properties and corresponding RAPINN losses for the bio-heat equation.

	Actual	**Loss of RAPINN on Bio-heat Equation**
Case	**Location & Diameter**	**Boundary Loss & Residual Loss**
L1S1	$(0.0, 0.0, 0.07),\ 10\ \mathrm{mm}$	1.5859×10^{0} & 4.1082×10^{2}
L1S2	$(0.0, 0.0, 0.07),\ 20\ \mathrm{mm}$	7.5557×10^{-1} & 4.6826×10^{2}
L2S1	$(0.0, 0.0, 0.04),\ 10\ \mathrm{mm}$	2.1180×10^{0} & 6.4505×10^{1}
L2S2	$(0.0, 0.0, 0.04),\ 20\ \mathrm{mm}$	2.0667×10^{0} & 4.2755×10^{1}
L3S1	$(0.0, 0.025, 0.07),\ 10\ \mathrm{mm}$	2.5486×10^{0} & 3.5346×10^{2}
L3S2	$(0.0, 0.025, 0.07),\ 20\ \mathrm{mm}$	7.9516×10^{-1} & 2.0874×10^{3}
No tumor	$(-, -, -),\ --$	6.5536×10^{0} & 5.4141×10^{0}

5.2 Inverse modeling

Table 3 reports the inverse estimation results: predicted tumor centers and diameters produced by RA-PINN, along with the characteristic loss components (boundary, residual and data losses). Inverse solutions were obtained by using the surface temperature maps from forward simulations as reference measurements.

Figure 14–16 presents a side-by-side comparison of inverse prediction, forward reference, and their difference for the healthy (no-tumor) case. The regression experiment for the healthy configuration produced a predicted z-coordinate below 0.01 m, consistent with no tumor detection. Recomputing the forward solution using the predicted parameters yields a surface temperature difference of approximately 0.2 K relative to the healthy reference, indicating the sensitivity of the measurement

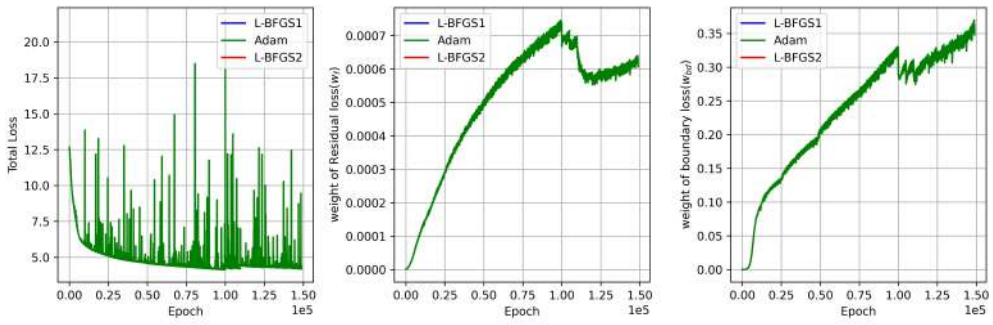

Figure 7: Total Loss and weights vs Epoch for L1S1

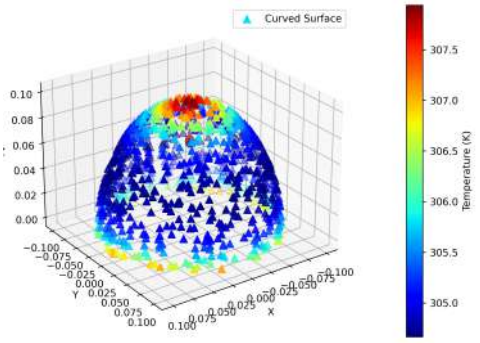

Figure 8: Surface temperature for L1S1

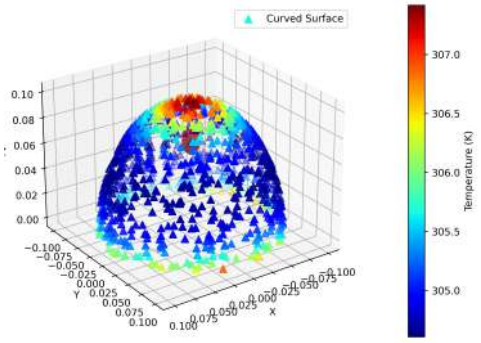

Figure 9: Surface temperature for L1S2

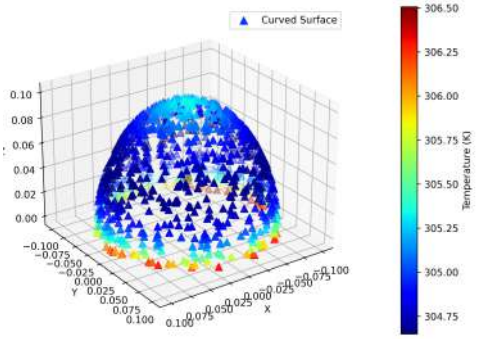

Figure 10: Surface temperature for L2S1

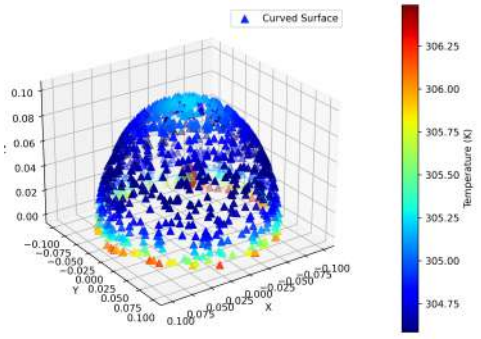

Figure 11: Surface temperature for L2S2

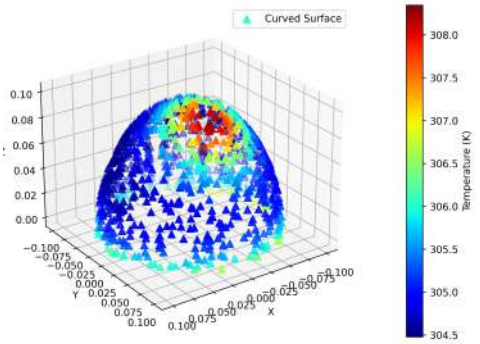

Figure 12: Surface temperature for L3S1

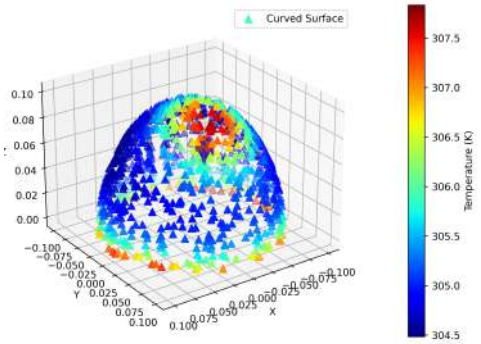

Figure 13: Surface temperature for L3S2

Table 3: RAPINN results (Bio-heat equation)

Case	Actual Location & Diameter	Predicted (RAPINN) Location & Diameter	Loss of RAPINN on Bio-heat Equation Boundary Loss & Residual Loss & Data Loss
L1S1	(0.0, 0.0, 0.07), 10 mm	[-1.2898e-05, 3.3805e-05, 7.0598e-02], [1.0068e-02]	1.7556e+00 & 6.8787e+01 & 1.6074e-05
L1S2	(0.0, 0.0, 0.07), 20 mm	[1.1403e-04, 1.5615e-04, 6.9961e-02], [1.9579e-02]	2.2171e+00 & 2.3708e+01 & 3.8977e-05
L2S1	(0.0, 0.0, 0.04), 10 mm	[-1.3010e-05, 2.3943e-05, 4.4957e-02], [1.2018e-02]	2.9540e+00 & 9.5481e+01 & 1.5163e-05
L2S2	(0.0, 0.0, 0.04), 20 mm	[2.6464e-04, 1.9953e-04, 4.2663e-02], [1.3228e-02]	2.6273e+00 & 6.0749e+01 & 2.1952e-05
L3S1	(0.0, 0.025, 0.07), 10 mm	[-4.6345e-05, 2.5465e-02, 7.1256e-02], [1.0115e-02]	3.2274e+00 & 3.9232e+01 & 3.5128e-05
L3S2	(0.0, 0.025, 0.07), 20 mm	[-2.3023e-05, 2.4134e-02, 6.8009e-02], [1.0480e-02]	1.3037e+00 & 1.3638e+02 & 3.3222e-05
No tumor	(-, -, -), - mm	[-8.5394e-05, -1.9895e-03, 7.5875e-03], [1.3815e-02]	1.0987e+01 & 1.1127e+01 & 1.1439e-05

setup. Representative inverse-vs-true comparisons for L1, L2 and L3 cases are displayed in Figures 17–22.

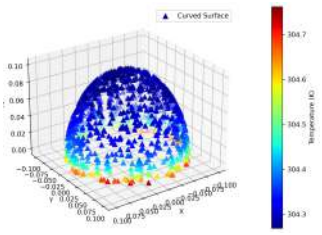

Figure 14: Inverse modeling of no-tumor case

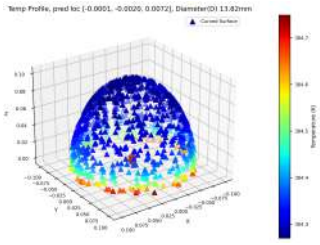

Figure 15: Forward result of healthy case

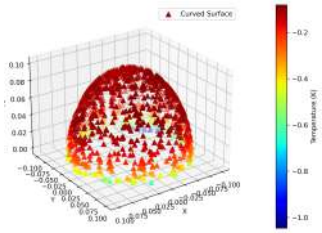

Figure 16: Temperature difference of inverse and forward result

Overall, RA-PINN delivers accurate forward temperature reconstructions and reliable inverse estimates within the tested parameter bounds; lateral-offset tumors present greater inverse uncertainty, highlighting the need for careful sensor placement or additional measurements in practical deployments.

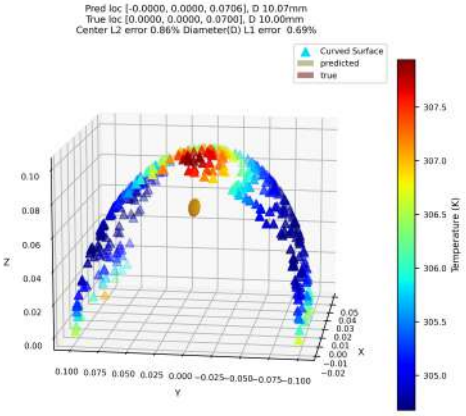

Figure 17: Inverse modeling for L1S1

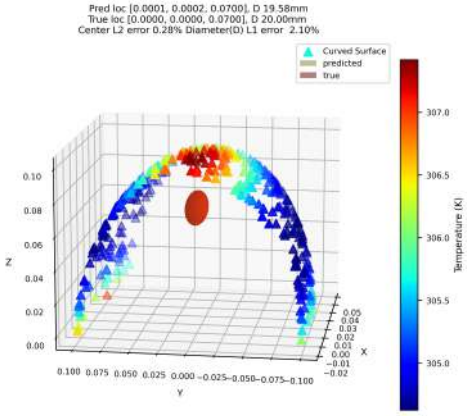

Figure 18: Inverse modeling for L1S2

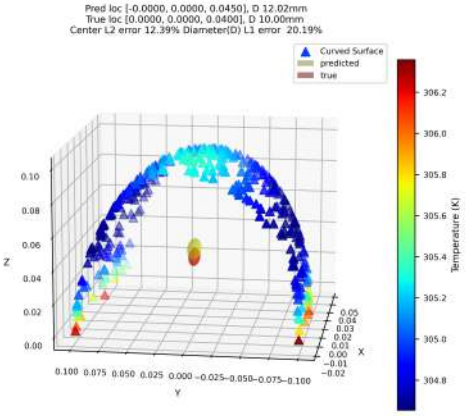

Figure 19: Inverse modeling for L2S1

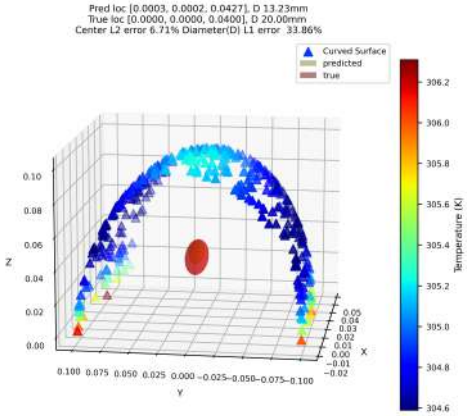

Figure 20: Inverse modeling for L2S2

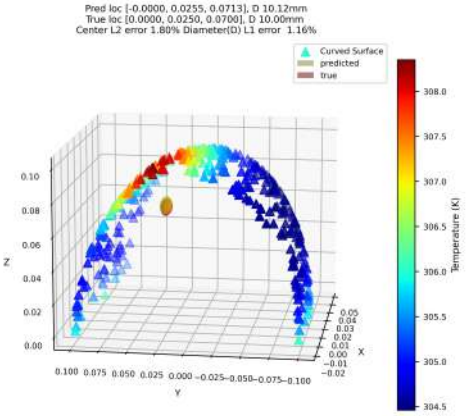

Figure 21: Inverse modeling for L3S1

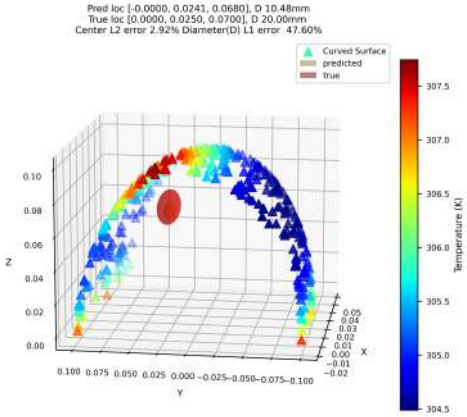

Figure 22: Inverse modeling for L3S2

6 Conclusion

This novel research work, RA-PINN, presents a robust computational framework for solving forward and inverse bioheat transfer problems with improved accuracy and efficiency in cancer detection and their localization. Designed for biomedical applications, the proposed architecture integrates the governing bioheat equation within a neural network structure, thereby enabling physics-guided learning of temperature distributions and underlying thermal parameters. By embedding data-driven flexibility with physical consistency, RA-PINN effectively addresses the limitations of conventional numerical methods and standard PINNs, particularly in handling parameter estimation and adaptive refinement.

The model demonstrates effective performance in breast thermal analysis, an application to noninvasive cancer detection, tumor localization, and shape estimation. Through adaptive loss balanced residual refinement, RA-PINN enhances detectability of tumor-induced thermal anomalies and significantly improves recovery of parameters. The evaluation metrics of the computational simulations underscore its reliability in modeling complex thermal patterns and present as an alternative tool to the invasive modalities.

In future work, attention score will be directed toward improving the scalability of the RA-PINN framework and also extending it to domain-decomposed configurations. Such developments will facilitate efficient simulation of large-scale, heterogeneous biological systems, enabling precise modeling of heat transfer in complex anatomical geometries. The integration of domain decomposition with RA-PINN is expected to enhance computational ability while maintaining high-resolution accuracy in localized regions of interest. Overall, this study establishes RA-PINN as a promising step toward the next generation of physics-informed, AI-driven biomedical modeling tools.

References

I. Perez-Rayaand c. Gutierrez and S. Kandlikar. A transformative approach for breast cancer detection using physics-informed neural network and surface temperature data. *ASME J. Heat Mass Transf.*, 146(10):101201, Jun 2024.

Suchuan Dong and Naxian Ni. A method for representing periodic functions and enforcing exactly periodic boundary conditions with deep neural networks. *Journal of Computational Physics*, 435:110242, 2021. ISSN 0021-9991. doi: https://doi.org/10.1016/j.jcp.2021.110242. URL `https://www.sciencedirect.com/science/article/pii/S0021999121001376`.

K. Ganesan, U. R. Acharya, C. K. Chua, L. C. Min, K. T. Abraham, and K. H. Ng. Computer-aided breast cancer detection using mammograms: a review. *IEEE Rev. Biomed. Eng.*, 6:77–98, 2012. doi: https://doi.org/10.1109/RBME.2012.2232289.

M. Gautherie. "thermopathology of breast cancer: Measurement and analysis of invivotemperatureandbloodflow. *Ann.N.Y.Acad.Sci.*, 1(335):383–415, 1980. doi: https://doi.org/10.1111/j.1749-6632.1980.tb50764.x.

J. L. Gonzalez-Hernandez, A. N. Recinella, S. G. Kandlikar, D. Dabydeen, L. Medeiros, and P. Phatak. An inverse heat transfer approach for patient-specific breast cancer detection and tumor localization using surface thermal images in the prone position. *Infrared Phys. Techn.*, 105:103202, 2020. doi: https://doi.org/10.1016/j.infrared.2020.103202.

C. Gutierrez and S. G. Kandlikar. Detectability of breast cancer through inverse heat transfer modeling using patient-specific surface temperatures. *J. Eng. Sci. Med. Diagn. Ther.*, 8(1), 2025. doi: https://doi.org/10.1115/1.4065797.

C. Gutierrez, A. Owens, L. Medeiros, D. Dabydeen, N. Sritharan, P. Phatak, and S. G. Kandlikar. Breast cancer detection using enhanced iri-numerical engine and inverse heat transfer modeling: model description and clinical validation. *Sci. Rep.*, 14(1):3316, 2024. doi: https://doi.org/10.1038/s41598-024-53856-w.

N. Harada-Shoji, A. Suzuki, T. Ishida, Y. F. Zheng, Y. Narikawa-Shiono, A. Sato-Tadano, R. Ohta, and N. Ohuchi. Evaluation of adjunctive ultrasonography for breast cancer detection among women aged 40–49 years with varying breast density undergoing screening mammography: a secondary analysis of a randomized clinical trial. *JAMA Netw. Open.*, 4(8):e2121505, 2021. doi: https://doi.org/10.1001/jamanetworkopen.2021.21505.

A. D. Jagtap and G. E. Karniadakis. Extended physics-informed neural networks (xpinns): A generalized space-time domain decomposition based deep learning framework for nonlinear partial differential equations. *Commun. Comput. Phys.*, 28(5):2002–2041, 2020. doi: https://doi.org/10.4208/cicp.OA-2020-0164.

D. P. Kingma and J. Ba. Adam: A method for stochastic optimization. *arXiv preprint arXiv:1412.6980*, 2014. doi: https://doi.org/10.48550/arXiv.1412.6980.

Quoc V. Le, Jiquan Ngiam, Adam Coates, Abhik Lahiri, Bobby Prochnow, and Andrew Y. Ng. On optimization methods for deep learning. In *Proc. 28th Int. Conf. Mach. Learn. (ICML)*, ICML'11, page 265–272, Madison, WI, USA, 2011. Omnipress. ISBN 9781450306195. URL https://dl.acm.org/doi/10.5555/3104482.3104516.

Revanth Mattey and Susanta Ghosh. A novel sequential method to train physics informed neural networks for allen cahn and cahn hilliard equations. *Computer Methods in Applied Mechanics and Engineering*, 390: 114474, 2022. ISSN 0045-7825. doi: https://doi.org/10.1016/j.cma.2021.114474. URL https://www.sciencedirect.com/science/article/pii/S0045782521006939.

Olzhas Mukhmetov, Yong Zhao, Aigerim Mashekova, Vasilios Zarikas, Eddie Yin Kwee Ng, and Nurduman Aidossov. Physics-informed neural network for fast prediction of temperature distributions in cancerous breasts as a potential efficient portable ai-based diagnostic tool. *Comput. Methods Programs Biomed.*, 242: 107834, 2023. ISSN 0169-2607.

M. N. Ozisik, H. R. Orlande, M. J. Colaco, and R. M. Cotta. *Finite Difference Methods in Heat Transfer*. CRC Press, 2017. doi: https://doi.org/10.1201/9781315121475.

Apostolos F Psaros, Kenji Kawaguchi, and George Em Karniadakis. Meta-learning pinn loss functions. *Journal of Computational Physics*, 458:111121, 2022. ISSN 0021-9991. doi: https://doi.org/10.1016/j.jcp.2022.111121. URL https://www.sciencedirect.com/science/article/pii/S0021999122001838.

M. Raissi, P. Perdikaris, and G. E. Karniadakis. Physics-informed neural networks: A deep learning framework for solving forward and inverse problems involving nonlinear partial differential equations. *J. Comput. Phys.*, 378:686–707, 2019. doi: https://doi.org/10.1016/j.jcp.2018.10.045.

G. Siravegna, S. Marsoni, S. Siena, and A. Bardelli. Integrating liquid biopsies into the management of cancer. *Nat. Rev. Clin. Oncol.*, 14(9):531–548, 2017. doi: https://doi.org/10.1038/nrclinonc.2017.14.

C. Wu, M. Zhu, Q. Tan, Y. Kartha, and L. Lu. A comprehensive study of non-adaptive and residual-based adaptive sampling for physics-informed neural networks. *Comput. Methods Appl. Mech. Engrg.*, 403:115671, 2023. doi: https://doi.org/10.1016/j.cma.2022.115671.

Z. Xiang, W. Peng, X. Liu, and W. Yao. Self-adaptive loss balanced physics-informed neural networks. *Neurocomputing*, 496:11–34, 2022. ISSN 0925-2312.

Jeremy Yu, Lu Lu, Xuhui Meng, and George Em Karniadakis. Gradient-enhanced physics-informed neural networks for forward and inverse PDE problems. *Computer Methods in Applied Mechanics and Engineering*, 393:114823, 2022. doi: https://doi.org/10.1016/j.cma.2022.114823.

Wei Zhou and YF Xu. Data-guided physics-informed neural networks for solving inverse problems in partial differential equations. *arXiv preprint arXiv:2407.10836*, 2024.